

# Dissecting stellar chemical abundance space with t-SNE

F. Anders<sup>1,2</sup>, C. Chiappini<sup>1,2</sup>, B. X. Santiago<sup>3,2</sup>, G. Matijević<sup>1</sup>, A. B. Queiroz<sup>3,2</sup>, B. Barbuy<sup>4,2</sup>

<sup>1</sup> Leibniz-Institut für Astrophysik Potsdam (AIP), An der Sternwarte 16, 14482 Potsdam, Germany  
e-mail: fanders@aip.de

<sup>2</sup> Laboratório Interinstitucional de e-Astronomia, - LIneA, Rua Gal. José Cristino 77, Rio de Janeiro, RJ - 20921-400, Brazil

<sup>3</sup> Instituto de Física, Universidade Federal do Rio Grande do Sul, Caixa Postal 15051, Porto Alegre, RS - 91501-970, Brazil  
<sup>4</sup> Universidade de São Paulo, IAG, Rua do Matão 1226, Cidade Universitária, 05508-900, São Paulo, Brazil

Received January 23, 2018; accepted ...

## ABSTRACT

2D chemical-abundance diagrams are important diagnostics of chemo-dynamical evolution in galaxies. However, in the era of industrial Galactic astronomy opened by multi-object spectroscopic stellar surveys, the sample sizes and the number of available abundances have reached dimensions in which it has become difficult to make use of all the available information in an effective manner. Here we demonstrate the use of t-distributed stochastic neighbour embedding (t-SNE) in spectroscopic stellar abundance space of the solar vicinity. By reanalysing high-resolution high-signal-to-noise solar-neighbourhood samples with t-SNE, we find clearer chemical separations of the high- and low-[ $\alpha$ /Fe] disc sequences, hints for multiple populations in the high-[ $\alpha$ /Fe] population, and a number of chemically peculiar stars, some of which were likely born in dwarf galaxies, others possibly in the Galactic bulge.

**Key words.** Galaxy: general – Galaxy: abundances – Galaxy: disk – Galaxy: stellar content – Stars: abundances

## 1. Introduction

One of the major goals of modern Galactic astrophysics is to infer the formation history of our Milky Way. To achieve this goal it is necessary to obtain precise 6D stellar kinematics as well as detailed chemical abundances for large stellar samples. This chemo-kinematical map of the Galactic stellar populations can then be compared to predictions of various Milky-Way models, eventually unveiling the star-formation and dynamical history of our Galaxy.

Massive spectroscopic observing campaigns such as RAVE (Steinmetz et al. 2006), SEGUE (Yanny et al. 2009), APOGEE (Majewski et al. 2017), LAMOST (Deng et al. 2012), GALAH (Martell et al. 2017) and the Gaia-ESO survey (Gilmore 2012) have in the past decade increased both the volume coverage and the statistical sample sizes by more than two orders of magnitude, to  $5 \cdot 10^6$  stars distributed from the solar vicinity to the far side of the Galactic bulge and the outer halo. In spite of this recent conquista of the Milky Way in terms of number of spectroscopically analysed stars, detailed multi-abundance chemo-kinematical studies of the immediate solar vicinity (Edvardsson et al. 1993; Fuhrmann 1998, 2011; Fuhrmann et al. 2017; Adibekyan et al. 2012; Bensby et al. 2014; Nissen 2015, 2016; Delgado Mena et al. 2017b, e.g.) remain at least equally important for Galactic Archaeology (see Lindegren & Feltzing 2013 for a quantitative analysis).

The wealth of new data, especially the high dimensionality of chemo-kinematics space, requires new statistical analysis methods to efficiently constrain detailed Milky-Way formation models (including e.g. stellar evolution, stellar chemical feedback, chemical evolution, and dynamical evolution). Traditionally, the metallicity distribution function and 2D chemical-abundance diagrams ([X/Fe] vs. [Fe/H]), and abundance gradients have been used to constrain the chemical evolution of stellar populations (e.g. Pagel 2009). On the other hand, it is also possible to define

a stellar population by chemistry (e.g. carbon-enhanced metal-poor stars - Beers & Christlieb 2005; the chemical thick disc - Gratton et al. 1996; Fuhrmann 1998; high-[ $\alpha$ /Fe] metal-rich stars - Adibekyan et al. 2011), and to then study their structural and chemo-kinematic properties in detail. This is usually done in a simple fashion, by looking at only one 2D abundance diagram. In this paper we explore the possibility of combining the information contained in various measured abundance ratios using t-distributed stochastic neighbour embedding (t-SNE) to define more robust subpopulations and better identify outliers.

In astronomical applications, t-SNE has mainly been used to identify objects with peculiar spectra (e.g. Matijević et al. 2017; Valentini et al. 2017; Traven et al. 2017). During the writing of this paper, Kos et al. (2017) demonstrated in a complementary analysis that abundance-space t-SNE is indeed a reliable chemical-tagging tool: the authors were able to recover 7 out of 9 known open and globular clusters with high efficiency and low contamination using 13 chemical abundances from the GALAH survey (Martell et al. 2017), and they also found two new field member stars to known clusters with this technique.

The paper is structured as follows: Sec. 2 introduces t-SNE. Sections 4 and 3 describe and discuss the results for the high-resolution spectroscopic solar-vicinity surveys of Bensby et al. (2014) and Delgado Mena et al. (2017b). We reconsider possible caveats of our results in Sec. 5 and finish with a summary and conclusions in Sec. 6.

## 2. Dissecting chemistry space with t-SNE

Interpreting the multi-dimensional abundance distributions determined by spectroscopic surveys is not a trivial task, since different abundance diagrams contain different nucleosynthetic information and may be affected by different observational errors. A convenient way to simplify this problem is dimension-

ality reduction, i.e. the projection of the N-dimensional abundance space onto a lower-dimensional space in which the chemical similarity between two stars is reflected by their distance in that space. Possibly the best-known such method is called principal component analysis (PCA), widely used also in astronomical literature. For highly-correlated datasets such as spectral pixel spaces or chemical-abundance spaces, however, more sophisticated non-linear methods like IsoMap or locally linear embedding are known to perform much better (e.g. Matijević et al. 2012; Ivezić et al. 2013).

In this paper, we reanalyse the high-resolution spectroscopic solar-vicinity surveys of Bensby et al. (2014) and Delgado Mena et al. (2017b) using a machine-learning algorithm called t-distributed stochastic neighbour embedding (t-SNE; Hinton & Roweis 2003; van der Maaten & Hinton 2008). This method is widely used in big-data analytics, and is able to efficiently project complex datasets onto a 2D plane in which the proximity between similar data points is preserved. We use the python implementation of t-SNE included in the `scikit-learn` package (Pedregosa et al. 2012) and refer to the original papers and the online documentation for details about the method and code. In short, the advantage of using t-SNE over other manifold-learning techniques is that it performs much better in revealing structure at many different scales (van der Maaten & Hinton 2008; Matijević et al. 2017), which is a necessary feature when looking for chemical substructure in the Galactic disc.

*How t-SNE works:* For a given set of  $N$  high-dimensional datapoints  $\mathbf{x}_1, \dots, \mathbf{x}_N$  (images, spectra, or in our case chemical-abundance vectors), t-SNE first computes pairwise similarity probabilities  $p_{ij}$  for the points  $\mathbf{x}_i$  and  $\mathbf{x}_j$ :

$$p_{j|i} = \frac{\exp(-\|\mathbf{x}_i - \mathbf{x}_j\|^2/2\sigma_i^2)}{\sum_{k \neq i} \exp(-\|\mathbf{x}_i - \mathbf{x}_k\|^2/2\sigma_i^2)}.$$

To circumvent problems with outliers, the symmetrised similarity of  $x_j$  and  $x_i$  is defined as

$$p_{ij} = \frac{p_{j|i} + p_{i|j}}{2N}.$$

In the next step, t-SNE attempts to learn a  $d$ -dimensional map  $\mathbf{y}_1, \dots, \mathbf{y}_N$  (in general  $d = 2$ ) that reflects the similarities  $p_{ij}$  similarities between two points  $\mathbf{y}_i$  and  $\mathbf{y}_j$  in the low-dimensional map, defined as

$$q_{ij} = \frac{(1 + \|\mathbf{y}_i - \mathbf{y}_j\|^2)^{-1}}{\sum_{k \neq m} (1 + \|\mathbf{y}_k - \mathbf{y}_m\|^2)^{-1}}.$$

This metric uses Student's  $t$  distribution to avoid crowding problems in the low-dimensional map (van der Maaten & Hinton 2008). Starting from a random Gaussian distribution in the  $d$ -dimensional map, the locations of the points  $\mathbf{y}_i$  are determined by minimizing the Kullback–Leibler divergence (Kullback & Leibler 1951) between the low- and high-dimensional similarity distributions  $Q$  and  $P$ :

$$KL(P||Q) = \sum_{i \neq j} p_{ij} \log \frac{p_{ij}}{q_{ij}},$$

using a gradient-descent method. The result of this optimization is a map that reflects the similarities between the high-dimensional inputs (see e.g. Fig. 1).

The method has one main parameter, the so-called perplexity,  $p$ , which governs the bandwidth of the Gaussian kernels  $\sigma_i$  appearing in the similarities  $p_{ij}$ . As a result, the bandwidth is adapted to the density of the data: smaller values of  $\sigma_i$  are used

in denser parts of the data space. The perplexity parameter can be thought of as a guess about the number of close neighbors each point has, and therefore the ideal value for  $p$  depends on the sample size. A change in perplexity has in many cases a complex effect on the resulting map, and different values for  $p$  should be explored (Wattenberg et al. 2016).

In addition, t-SNE, as a genuine machine-learning technique, does have two drawbacks that are relevant for our science case. First, it does not account for individual uncertainties, and may therefore be affected by extremely heteroscedastic errors. Secondly, its current implementations do not allow to treat missing data, so that any star with a missing individual abundance measurement has to be excluded.

### 3. Re-analysing the HARPS GTO sample

In a recent series of papers, Adibekyan et al. (2011, 2012); Delgado Mena et al. (2014, 2015); Bertran de Lis et al. (2015); Suárez-Andrés et al. (2017); Delgado Mena et al. (2017b,a) studied the chemical abundances of a sample of 1111 solar-vicinity FGK stars using the very high resolution of the HARPS spectrograph ( $R \sim 115,000$ ). This sample mostly contains metal-rich warm dwarf and subgiant stars, but also includes a wide range of effective temperatures, gravities and metallicities. Delgado Mena et al. (2017b) reanalysed this sample, employing a revised linelist (Tsantaki et al. 2013), improving the effective temperature calibration, and correcting spectroscopic gravities using the *Hipparcos* parallaxes of van Leeuwen (2007). They report chemical abundances for Mg, Al, Si, Ca, Ti, Fe, Cu, Zn, Sr, Y, Zr and Ba for 1059 stars (Ce, Nd and Eu are available for a substantial subset of these), derived using standard Local Thermodynamic Equilibrium (LTE) analysis using ARES to measure equivalent widths and MOOG to measure abundances by comparing to Kurucz ATLAS9 atmospheres. In this section we test the performance of abundance-space t-SNE on this most recent HARPS GTO sample compilation.

Our first tests showed that, in order to obtain reliable t-SNE abundance maps, the sample needed to be analysed in a more restricted temperature range, because certain abundance trends seem to be dominated by underlying temperature trends. Therefore, and similar to Delgado Mena et al. (2017b), we chose an effective temperature range of  $5300 \text{ K} < T_{\text{eff}} < 6000 \text{ K}$  for our analysis. We furthermore restricted surface gravities to  $3 < \log g_{\text{HIP}} < 5$ , required successful abundance determination for Mg, Al, Si, Ca, TiII, Fe, Cu, Zn, Sr, Y, ZrII, Ce and Ba that we use as input for t-SNE, leaving us with 533 stars. In our final sample of 530 stars we also discarded 3 stars for which our age determination code, StarHorse (Santiago et al. 2016; Queiroz et al. 2017), did not converge(?). We verified that this choice does not significantly affect the resulting t-SNE maps.

The chemical abundances were complemented by astrometric data (parallaxes, proper motions) from the Gaia/TGAS catalogue Gaia Collaboration et al. (2016), or when these were unavailable (135/1059 stars), from the re-reduced *Hipparcos* data (van Leeuwen 2007).

Before we analyse the t-SNE results, some important differences of the HARPS GTO sample with respect to the Bensby sample should be stressed:

- the absence of kinematic selection biases: The HARPS sample initially served to detect and characterise exoplanets and may therefore contain some metallicity-related selection bias; however, e.g. Anders et al. (2014) have shown that the HARPS metallicity distribution (MDF) matches the MDF of



**Fig. 1.** t-SNE projection ( $p = 40$ ) of the Delgado Mena et al. (2017b) sample, colour-coded by chemical abundances (top three rows), stellar atmospheric parameters and signal-to-noise ratio (fourth row), age (fifth row, first panel) and UVW velocities (fifth row). We note that only [Fe/H] and the [X/Fe] ratios were used as input for the t-SNE run. The distinct populations appearing in these diagrams are studied in detail in Fig. 2.

high-quality local ( $d < 1$  kpc) APOGEE red-giant stars that could be considered less chemically biased. In contrast to the Bensby et al. (2014) sample, it was not targeted based on kinematic priors.

- the availability of different abundances: O, Na, V, Cr, Co and Ni are only available for the Bensby sample, while Sr, Zr and Ce are only available for the HARPS sample. Carbon estimates are available from a previous study (Suárez-Andrés et al. 2017), but since they are based on previous stellar parameter estimates, we decided to only use them in the interpretation. We also did not use Nd and Eu, and the O estimates from Bertran de Lis et al. (2015) in the t-SNE run, because

they were only available for about half of the sample (stars with the highest signal-to-noise ratios). We do, however, use the Nd and Eu results in the interpretation, whenever they are available.

Fig. 1 shows our reference t-SNE map for the HARPS sample, colour-coded in a similar way as Fig. 5, by chemical-abundance ratios, stellar parameters, ages and kinematics. Again, the panels coloured as a function of stellar parameters indicate that the sample is not affected by major systematic abundance trends with stellar parameters, since we focus on a narrow

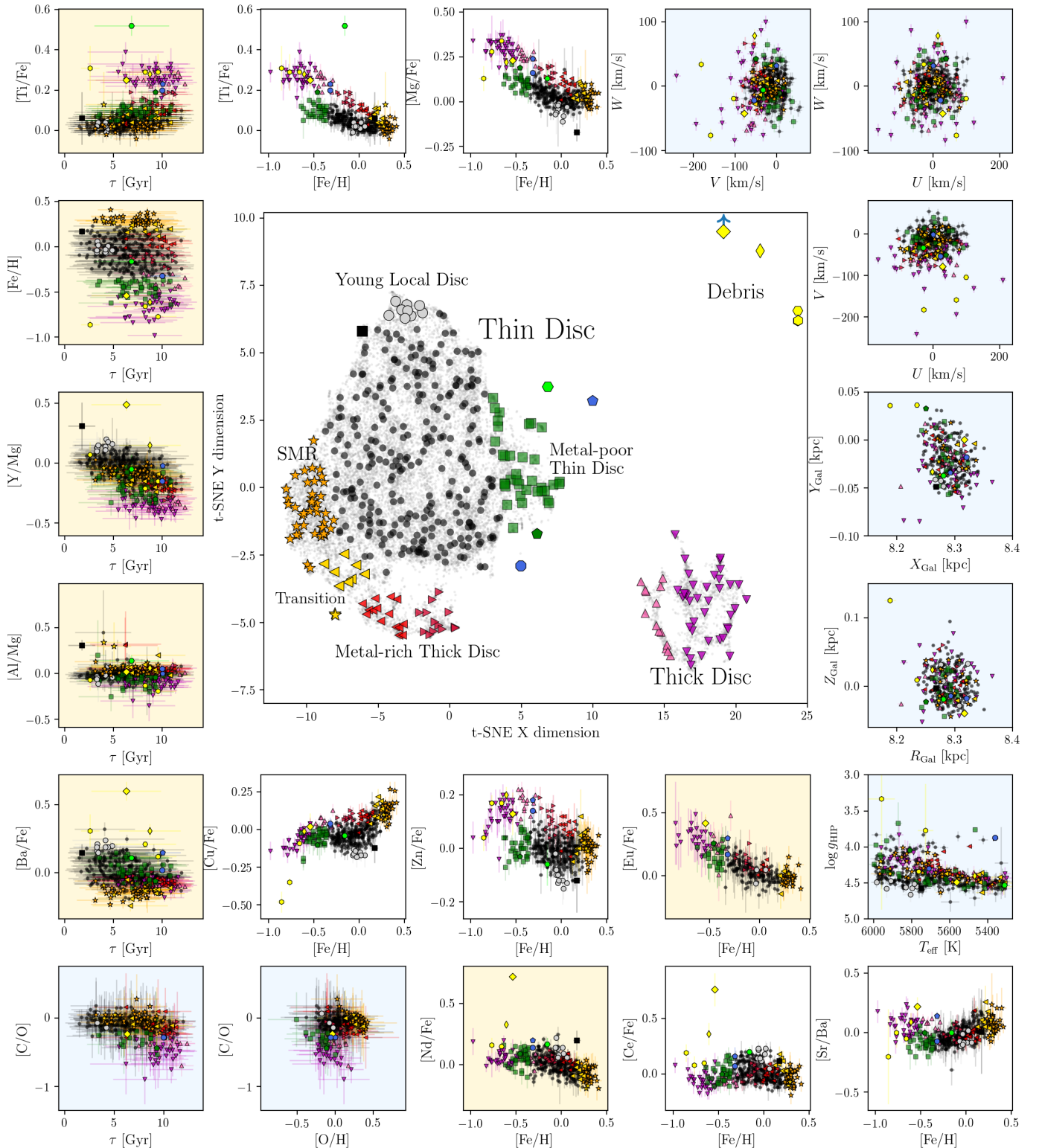


**Fig. 2.** The chemo-chrono-kinematic distribution of t-SNE-selected subsamples of the Delgado Mena et al. (2017b) sample, in a similar style as Fig. 6.

region in parameter space. As argued in Sec. 4, we did not apply any ad-hoc corrections to the reported abundances.

Following the methodology of Sec. 4, we again identify some of the substructures that appear in Fig. 1 in Fig. 2. Fig. 3 shows the corresponding  $[X/\text{Fe}]$  abundance trends versus pro-

ton number for each of those substructures. We now proceed to the discussion of each substructure, bearing in mind our findings of Sec. 4:

*The overall appearance of the t-SNE map:* Since t-SNE is a highly non-linear projection method, and since sample and its

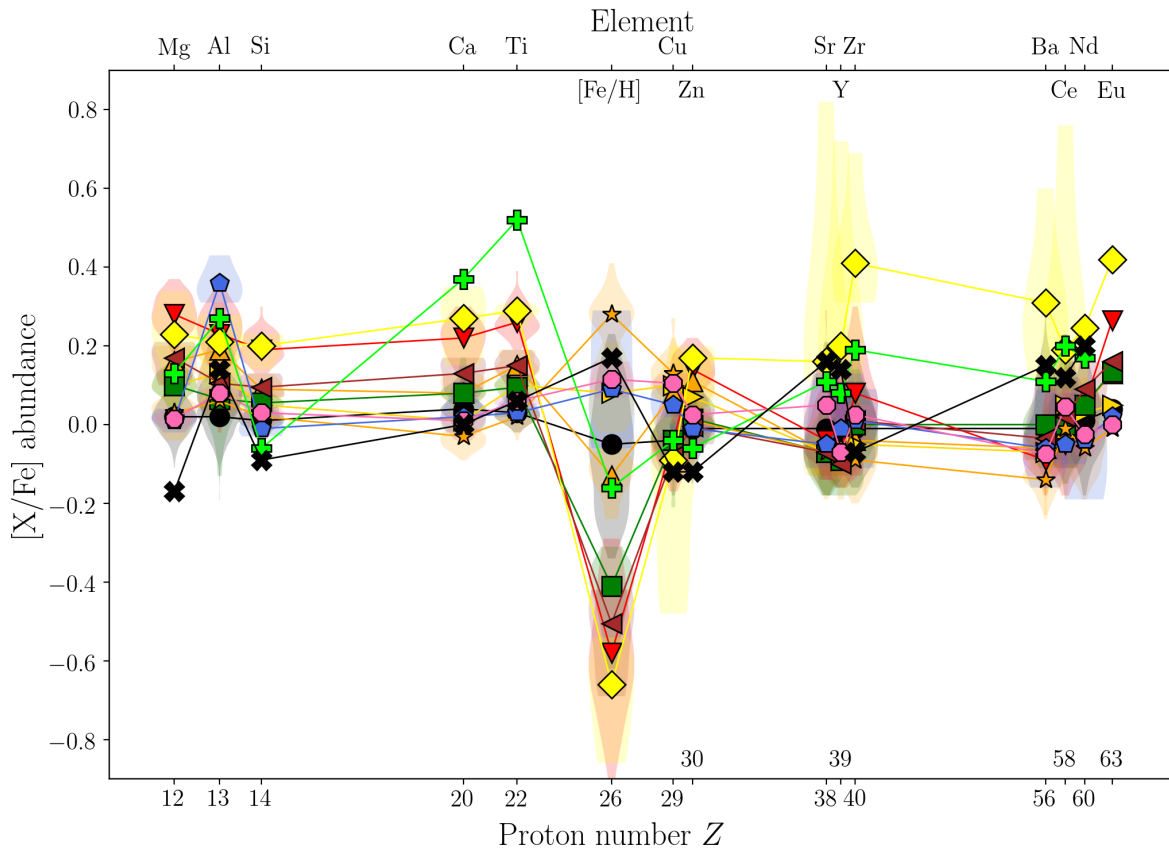


**Fig. 3.** Chemical-abundance patterns relative to iron for the t-SNE-selected subsamples of the HARPS survey (colours and symbols as in Fig. 2, but note that the reference abundance is Fe instead of O). For visibility, we show only the median abundance ratios of each group.

abundance determination method differ significantly from the stars studied by Bensby et al. (2014), the overall morphologies of the t-SNE maps in Figs. 5 and 1 are also expected to be dissimilar. While this is indeed the case, there are some features that appear in both maps, and can therefore be suggested to be generic properties of the solar-neighbourhood abundance space:

*The thin-thick dichotomy:* As discussed in the works of Adibekyan et al. (2011, 2012) or Delgado Mena et al. (2017b), there is a clear discontinuity between the high- and the low-[ $\alpha$ /Fe] sequences in the [Mg/Fe] vs. [Fe/H] diagram. As in the case of the Bensby sample, this discontinuity is reflected in a very clear manner in the t-SNE projection.

*Three clear thick-disc sub-populations:*

*Thin-thick transition stars:*

*Super-metal-rich stars:*

*The metal-poor thin disc:*

*Other potential groups and substructures in the thin disc:*

*Satellite debris:*

#### 4. Re-analysing the Bensby et al. (2014) sample

Bensby, Feltzing, & Oey (2014) studied the chemistry and kinematics of 714 FGK stars in the *Hipparcos* volume. Their sample was selected based on kinematic criteria that enabled the authors to explicitly study the metal-poor tail of the disc and its transition to the halo, as well as the metal-rich end of the thick disc. Using high-resolution optical spectroscopy, they report chemical abundances for the 13 elements O, Na, Mg, Al, Si, Ca, Ti, Cr, Fe,

Ni, Zn, Y and Ba. This high number of measured abundances, in conjunction with the high precision of the measurements and the reasonable sample size, makes the Bensby sample an ideal test case for our machine-learning algorithm. However, since t-SNE cannot cope with missing data, we select only the 600 stars for which all these abundances were available for our analysis, which results in a lower metallicity limit of [O/H] > -0.8. Since our main interest here is in the chemical substructure of the disc, this requirement does not hinder our analysis.

In Fig. 5, we again show the selected t-SNE plane from Fig. 4, but now colour-coded by chemical-abundance ratios, stellar parameters, ages and kinematics. The panels in the first three rows show how t-SNE is grouping the stars with similar abundances in the two-dimensional plane. The panels coloured as a function of stellar parameters demonstrate that the sample is not subject to major systematic abundance shifts, but does show some residual trends with effective temperature, since it preferentially groups cooler stars in slightly different regions of the t-SNE map than hotter ones. Because part of this effect may be due to chemical evolution rather than systematic abundance errors, we decided not to apply any ad-hoc corrections to the abundances.

In Fig. 6 we identify some of the substructures that appear in Fig. 5, and discuss them below. In addition, Fig. 7 shows the corresponding [X/O] abundance trends versus proton number, for each of the subpopulations defined in Fig. 6.

*The thin-thick discontinuity:* We find a clear and obvious dichotomy of thin and thick disc in the t-SNE diagram (upper left

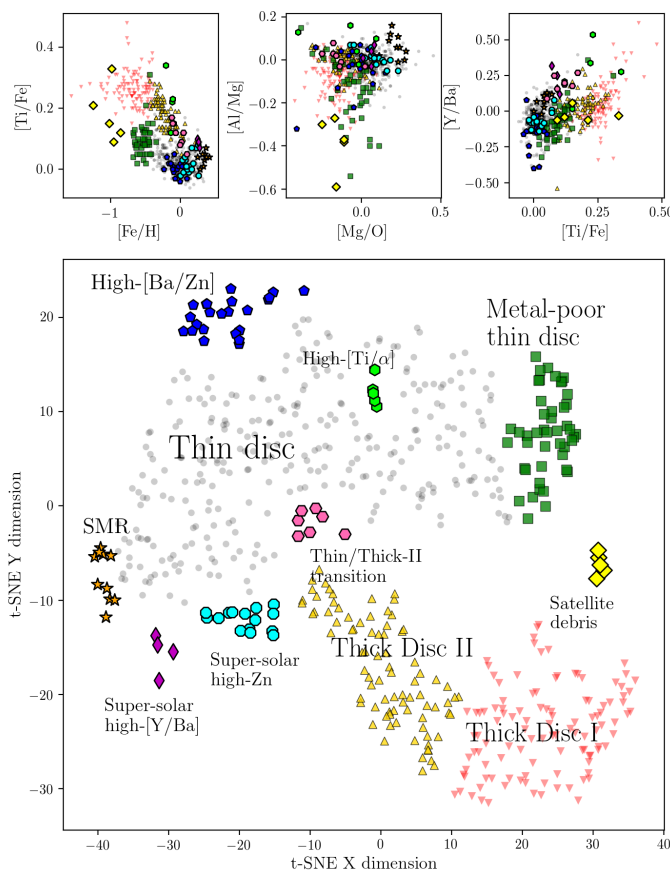


**Fig. 4.** Illustration of how t-SNE works, using the Bensby et al. (2014) survey. The top row shows three of the possible  $\sim 20,000$  abundance diagrams that can be created from 13 elements. The resulting reference t-SNE projection of the full abundance space is shown in the bottom panel, and several identified subgroups are indicated.

vs. lower right) that remains robust for different choices of the perplexity value. Primarily, this means that the chemical patterns of thin and thick disc are indeed distinct, and can be disentangled by high-resolution spectroscopy. Secondly, our analysis of the full chemical information results in a much more accurate division of the chemically-thin and thick populations. Indeed, if one only relies on one diagnostic, such as the  $[\text{Ti}/\text{Fe}]$  vs.  $[\text{Fe}/\text{H}]$  diagram (Bensby et al. 2014), several stars (e.g. thin-disc stars that have an unusual  $[\text{Ti}/\alpha]$  ratio – limegreen hexagons in Fig. 6, or low- $[\text{Fe}/\text{H}]$  thin disc stars – green squares) will be incorrectly identified as chemical thick disc.

*hamr stars & substructure in the thick disc:* Adibekyan et al. (2011) first discovered a clear discontinuity between the metal-poor and metal-rich  $[\alpha/\text{Fe}]$ -enhanced (or hamr) disc populations. In our t-SNE analysis of the Bensby et al. (2014) sample, similar to the original paper, we only see a hint of a difference between the two populations (dubbed Thick Disc I and II in Fig. 5). The bimodality is better seen when slightly higher perplexity values are chosen ( $p \sim 30$ ). Even if ages and/or kinematics are included as additional dimensions in the analysis, this picture does not change much.

*Thin-thick transition:* Most literature measurements agree that the high- and low- $[\alpha/\text{Fe}]$  sequences in the  $[\alpha/\text{Fe}]$  vs.  $[\text{Fe}/\text{H}]$  diagram merge at super-solar metallicities (e.g. Adibekyan et al. 2011; Anders et al. 2014; Hayden et al. 2015). In other words, the upper metallicity limit of the high- $[\alpha/\text{Fe}]$  or the hamr population is not yet firmly established. Our analysis shows that including

the full chemistry information does not allow us to completely solve this question, since the border between thin-disc-like and thick-disc-like chemistry remains debatable in the t-SNE projection (e.g. the pink hexagons in Fig. 5 have intermediate characteristics between Thick Disc II and Thin disc).

*Super-metal-rich stars:* SMR stars ( $[\text{Fe}/\text{H}] > 0.3$  – the western-most stars in the t-SNE plane; orange stars in Fig. 6) have only slightly different abundance patterns from the bulk of the thin disc stars (grey dots): they are slightly enhanced in  $[\text{Y}/\text{Ba}]$ , for example, and slightly  $[\text{Ti}/\text{Fe}]$ -enhanced with respect to the thin disc, indicative of an origin in the inner Milky-Way disc. All but one have ages smaller than 5 Gyr, and are on cold orbits ( $e < 0.12$ ), which means that they have likely suffered from radial migration (see e.g. Minchev et al. 2012; Vera-Ciro et al. 2014; Kordopatis et al. 2015; Grand & Kawata 2016; Anders et al. 2017).

*The metal-poor thin disc:* The green squares in Fig. 6 correspond to the metal-poor thin disc ( $[\text{Fe}/\text{H}] \sim -0.5$ ). Apart from metallicity, its main abundance differences with respect to the bulk of the chemical thin-disc population are: 1. a light elevation of  $[\alpha/\text{Fe}]$ , as a consequence of the slower star-formation history in the outer disc, where this population is most likely to originate from (e.g. Anders et al. 2014; Hayden et al. 2015; see also kinematic diagnostics in Fig. 6, especially the eccentricity-mean radius diagram), 2. a systematic deficiency in  $[\text{Al}/\text{Mg}]$ , in conjunction with a rather striking correlation between  $[\text{Al}/\text{Mg}]$  and age for this group. A strong correlation between age and  $[\text{Al}/\text{Mg}]$  has recently been found in solar-metallicity solar twins (Nissen 2015, 2016; Tucci Maia et al. 2016; Nissen et al. 2017). Here we find that this correlation persists for a broader range of stellar parameters, lower signal-to-noise ratios, and more uncertain age estimates, and appears much stronger for the metal-poor thin-disc stars.

*Other potential groups and substructures in the thin disc:* In Fig. 6 we also highlight several other smaller groups of stars that can be viewed as sub-populations of the chemical thin disc, but are peculiar in some respect. These are: a) a group of stars with high zinc abundances (cyan octagons), but otherwise typical thin-disc-like abundances (see Fig. 7); b) a group of four SMR stars ( $[\text{Fe}/\text{H}] \approx 0.2$ ,  $[\text{O}/\text{H}] \approx 0.25$ ) with slightly elevated  $[\text{Y}/\text{Ba}]$ ,  $[\text{Ti}/\text{Fe}]$ , and  $[\text{O}/\text{Mg}]$  abundance ratios (with respect to stars of similar metallicities); c) a group of slightly s-process-enhanced solar-metallicity stars (most notably enhanced in  $[\text{Ba}/\text{Zn}]$ ; blue pentagons); and a group of five stars with enhanced  $[\text{Ti}/\alpha]$ ,  $[\text{Al}/\text{Mg}]$ , and  $[\text{Y}/\text{Ba}]$  ratios (limegreen hexagons). A detailed discussion of these objects is likely premature, but our results, in conjunction with the cluster experiment of Kos et al. (2017), already demonstrate the potential of t-SNE for chemical-tagging studies.

*Satellite debris:* Another observation of Fig. 6 is that our method clearly singles out a small group of five stars with dwarf-galaxy or globular-cluster-like abundance pattern (some more were lost due to the abundance quality cut). These five stars (HIP 34285, HIP 55592, HIP 58962, HIP 61802, HIP 90261; yellow diamonds in Fig. 6) are all on highly eccentric orbits, have low  $[\text{Al}/\text{Mg}]$  and high  $[\text{Zn}/\text{O}]$  abundances, and four of them are  $[\text{Ti}/\text{Fe}]$ -poor, placing them in the typical dwarf-galaxy regime.

## 5. Caveats and possible improvements

### 5.1. Choosing the abundance space

The t-SNE results for the Bensby et al. (2014) dataset are shown in Fig. 8, for a range of perplexity values and different input.

t-SNE manifold learning for the Bensby+2014 sample

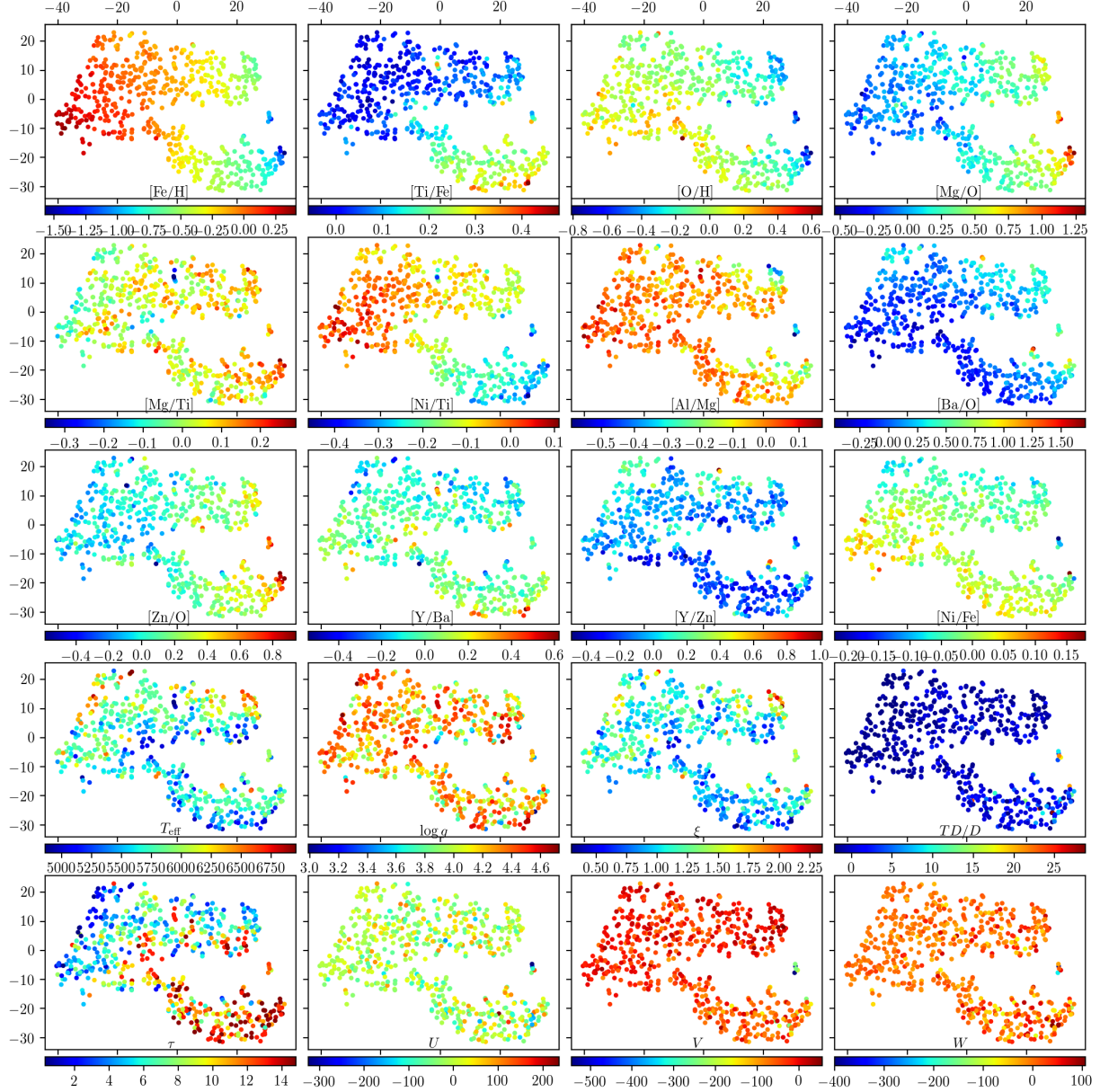


**Fig. 5.** t-SNE projection ( $p = 15$ ) of the Bensby et al. (2014) sample, colour-coded by chemical abundances (top three rows), stellar atmospheric parameters (fourth row), thick-to-disc probability (fourth row, last panel), age (fifth row, first panel) and UVW velocities (fifth row). We note that only  $[Fe/H]$  and the  $[X/Fe]$  ratios were used as input for the t-SNE run. The distinct populations appearing in these diagrams are studied in detail in Fig. 6.

Following the recommendations of van der Maaten & Hinton (2008) and Wattenberg et al. (2016), we use this figure to choose the optimal perplexity value for each dataset (yellow-highlighted panels). In the following subsections, we analyse these results in detail.

## 5.2. Residual trends with stellar parameters

## 5.3. The effect of adding age and kinematics to the analysis

## 6. Conclusions

YES WE CAN use t-SNE to better define subpopulations in abundance space. However, the non-parametric non-linear behaviour of the technique makes it difficult to estimate the significance of found subgroups or clusters. The method could, however, be coupled to a genuine cluster finding algorithm.

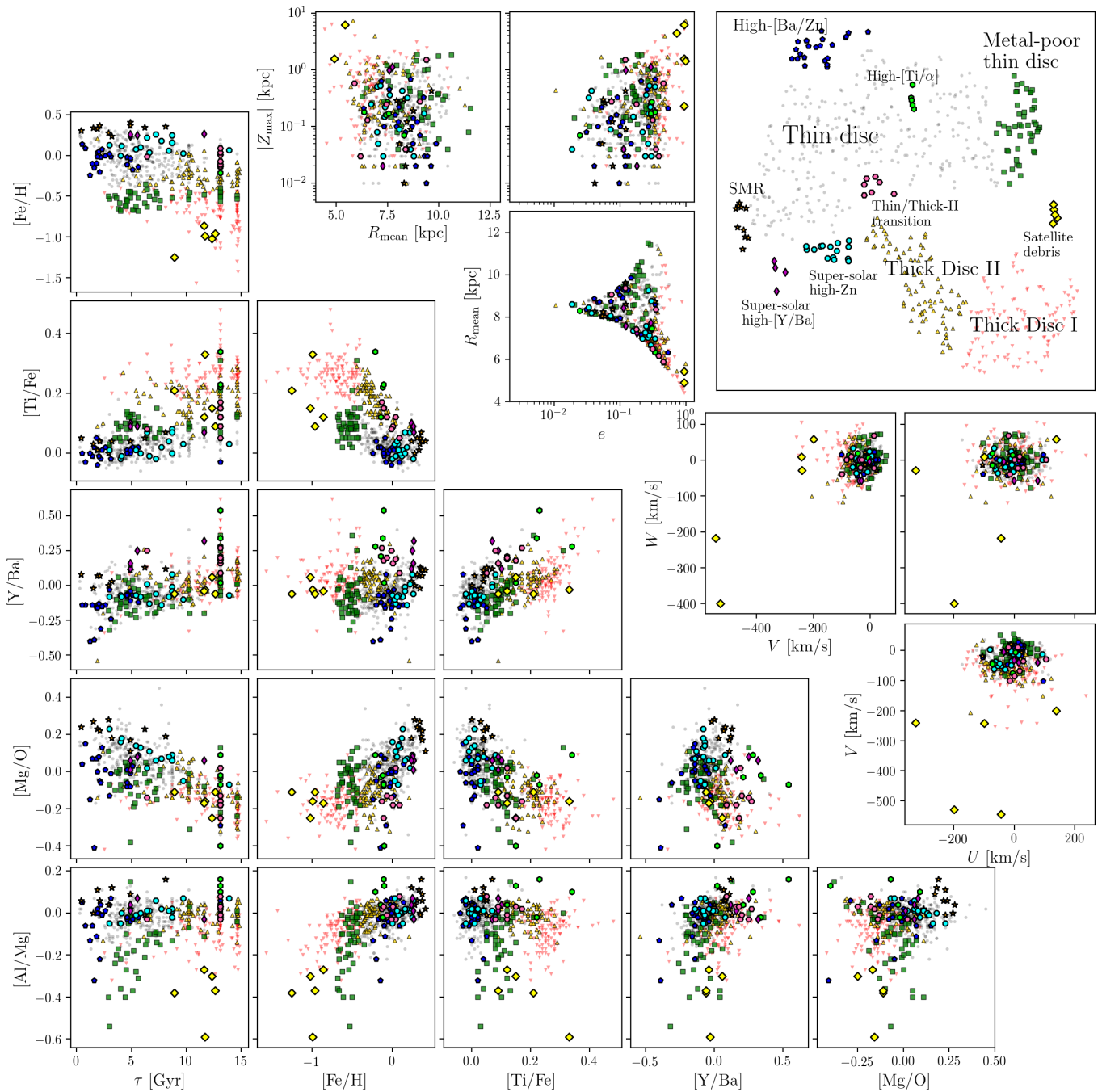


**Fig. 6.** The chemo-chrono-kinematic distribution of t-SNE-selected subsamples of the Bensby et al. (2014) survey. The definition of the subsets in the t-SNE plane is shown in the top right panel. The big corner plot shows the 2D correlations between age and five representative chemical abundance ratios, while the small corner plots correspond to velocity and orbital-parameter correlations.

Potential for weak chemical tagging demonstrated in this paper; the viability of t-SNE for strong chemical tagging (finding dispersed members of open clusters) is still not completely clear, but see Kos et al. (2017).

It is better to confine the analysis to narrow regions in atmospheric-parameter space to avoid spurious abundance trends induced by differences in atmospheric parameters.

## References

- Adibekyan, V. Z., Santos, N. C., Sousa, S. G., & Israelian, G. 2011, A&A, 535, L11  
 Adibekyan, V. Z., Sousa, S. G., Santos, N. C., et al. 2012, A&A, 545, A32  
 Anders, F., Chiappini, C., Rodrigues, T. S., et al. 2017, A&A, 597, A30  
 Anders, F., Chiappini, C., Santiago, B. X., et al. 2014, A&A, 564, A115  
 Beers, T. C. & Christlieb, N. 2005, ARA&A, 43, 531  
 Bensby, T., Feltzing, S., & Oey, M. S. 2014, A&A, 562, A71  
 Bertran de Lis, S., Delgado Mena, E., Adibekyan, V. Z., Santos, N. C., & Sousa, S. G. 2015, A&A, 576, A89  
 Delgado Mena, E., Bertran de Lis, S., Adibekyan, V. Z., et al. 2015, A&A, 576, A69  
 Delgado Mena, E., Israelian, G., González Hernández, J. I., et al. 2014, A&A, 562, A92  
 Delgado Mena, E., Tsantaki, M., Adibekyan, V. Z., et al. 2017a, ArXiv e-prints  
 Delgado Mena, E., Tsantaki, M., Adibekyan, V. Z., et al. 2017b, ArXiv e-prints  
 Deng, L.-C., Newberg, H. J., Liu, C., et al. 2012, Research in Astronomy and Astrophysics, 12, 735

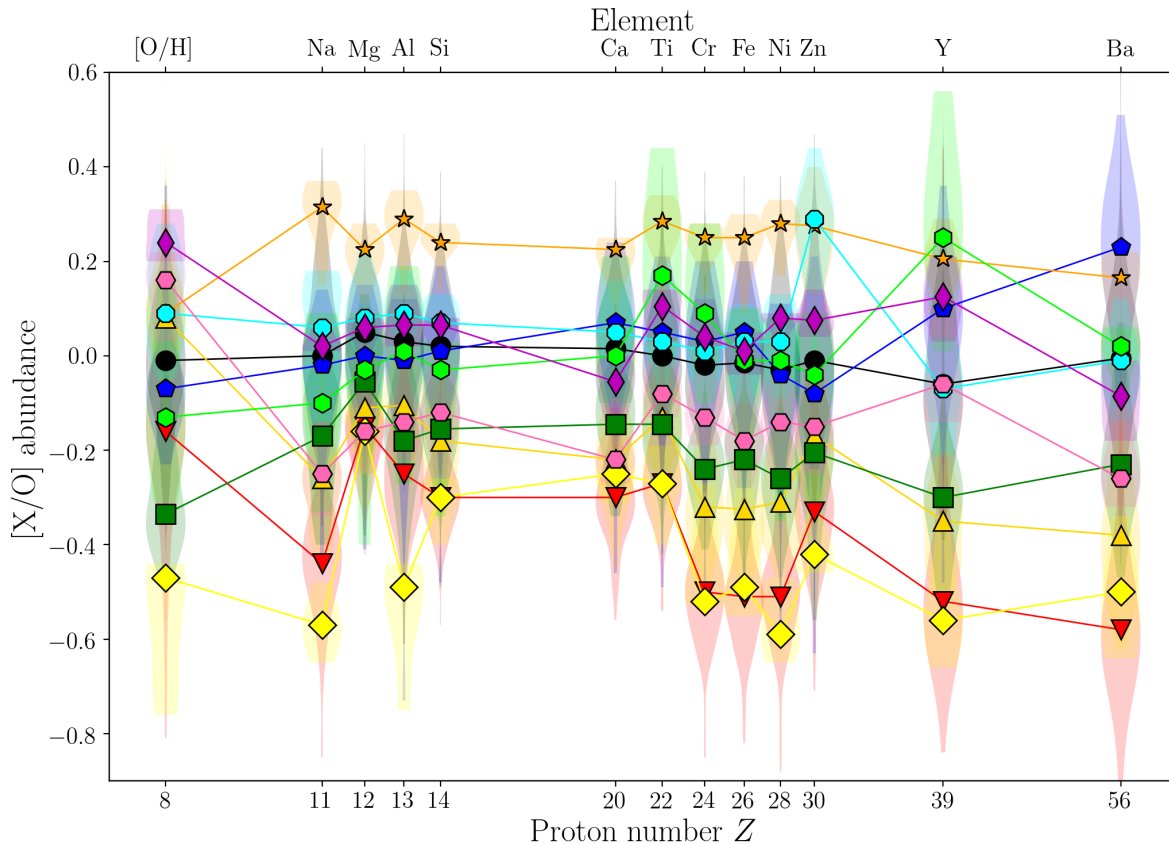


**Fig. 7.** Chemical-abundance patterns relative to oxygen for the t-SNE-selected subsamples of the Bensby et al. (2014) survey (colours and symbols as in Fig. 6). For visibility, we show only the median abundance ratios of each group.

- Edvardsson, B., Andersen, J., Gustafsson, B., et al. 1993, *A&A*, 275, 101  
 Fuhrmann, K. 1998, *A&A*, 338, 161  
 Fuhrmann, K. 2011, *MNRAS*, 414, 2893  
 Fuhrmann, K., Chini, R., Kaderhandt, L., & Chen, Z. 2017, *MNRAS*, 464, 2610  
 Gaia Collaboration, Brown, A. G. A., Vallenari, A., et al. 2016, *A&A*, 595, A2  
 Gilmore, G. 2012, in *Astronomical Society of the Pacific Conference Series*, Vol. 458, Galactic Archaeology: Near-Field Cosmology and the Formation of the Milky Way, ed. W. Aoki, M. Ishigaki, T. Suda, T. Tsujimoto, & N. Arimoto, 147  
 Grand, R. J. J. & Kawata, D. 2016, *Astronomische Nachrichten*, 337, 957  
 Gratton, R., Carretta, E., Matteucci, F., & Sneden, C. 1996, in *Astronomical Society of the Pacific Conference Series*, Vol. 92, Formation of the Galactic Halo...Inside and Out, ed. H. L. Morrison & A. Sarajedini, 307  
 Hayden, M. R., Bovy, J., Holtzman, J. A., et al. 2015, *ApJ*, 808, 132  
 Hinton, G. E. & Roweis, S. T. 2003, in *Advances in neural information processing systems*, 857–864  
 Ivezić, Ž., Connolly, A., VanderPlas, J., & Gray, A. 2013, *Statistics, Data Mining, and Machine Learning in Astronomy*  
 Kordopatis, G., Binney, J., Gilmore, G., et al. 2015, *MNRAS*, 447, 3526  
 Kos, J., Bland-Hawthorn, J., Freeman, K., et al. 2017, *MNRAS*, submitted, arXiv:1709.00794  
 Kullback, S. & Leibler, R. A. 1951, *Ann. Math. Statist.*, 22, 79  
 Lindegren, L. & Feltzing, S. 2013, *A&A*, 553, A94  
 Majewski, S. R., Schiavon, R. P., Frinchaboy, P. M., et al. 2017, *AJ*, 154, 94  
 Martell, S. L., Sharma, S., Buder, S., et al. 2017, *MNRAS*, 465, 3203  
 Matijević, G., Chiappini, C., Grebel, E. K., et al. 2017, *A&A*, 603, A19  
 Matijević, G., Zwitter, T., Bienaymé, O., et al. 2012, *ApJS*, 200, 14  
 Minchev, I., Famaey, B., Quillen, A. C., et al. 2012, *A&A*, 548, A127  
 Nissen, P. E. 2015, *A&A*, 579, A52  
 Nissen, P. E. 2016, *A&A*, 593, A65  
 Nissen, P. E., Silva Aguirre, V., Christensen-Dalsgaard, J., et al. 2017, ArXiv e-prints  
 Pagel, B. E. J. 2009, *Nucleosynthesis and Chemical Evolution of Galaxies*  
 Pedregosa, F., Varoquaux, G., Gramfort, A., et al. 2012, ArXiv e-prints  
 Queiroz, A. B. A., Anders, F., Santiago, B. X., et al. 2017, *MNRAS*, submitted, arXiv:1710.09970  
 Santiago, B. X., Brauer, D. E., Anders, F., et al. 2016, *A&A*, 585, A42  
 Steinmetz, M., Zwitter, T., Siebert, A., et al. 2006, *AJ*, 132, 1645  
 Suárez-Andrés, L., Israelian, G., González Hernández, J. I., et al. 2017, *A&A*, 599, A96  
 Traven, G., Matijević, G., Zwitter, T., et al. 2017, *ApJS*, 228, 24  
 Tsantaki, M., Sousa, S. G., Adibekyan, V. Z., et al. 2013, *A&A*, 555, A150  
 Tucci Maia, M., Ramírez, I., Meléndez, J., et al. 2016, *A&A*, 590, A32  
 Valentini, M., Chiappini, C., Davies, G. R., et al. 2017, *A&A*, 600, A66  
 van der Maaten, L. & Hinton, G. 2008, *The Journal of Machine Learning Research*, 9, 85  
 van Leeuwen, F., ed. 2007, *Astrophysics and Space Science Library*, Vol. 350, Hipparcos, the New Reduction of the Raw Data  
 Vera-Ciro, C., D’Onghia, E., Navarro, J., & Abadi, M. 2014, *ApJ*, 794, 173  
 Wattenberg, M., Viégas, F., & Johnson, I. 2016, Distill  
 Yanny, B., Rockosi, C., Newberg, H. J., et al. 2009, *AJ*, 137, 4377

*Acknowledgements.* FA would like to thank Elisa Delgado-Mena for sharing the HARPS-GTO data with us, and Guillaume Guiglion, Katia Cunha, Paula Jofré, Bertrand Lemasle and the other participants of the IAU symposium 334 in Potsdam, as well as David W. Hogg, for their encouragement and/or critical thoughts.

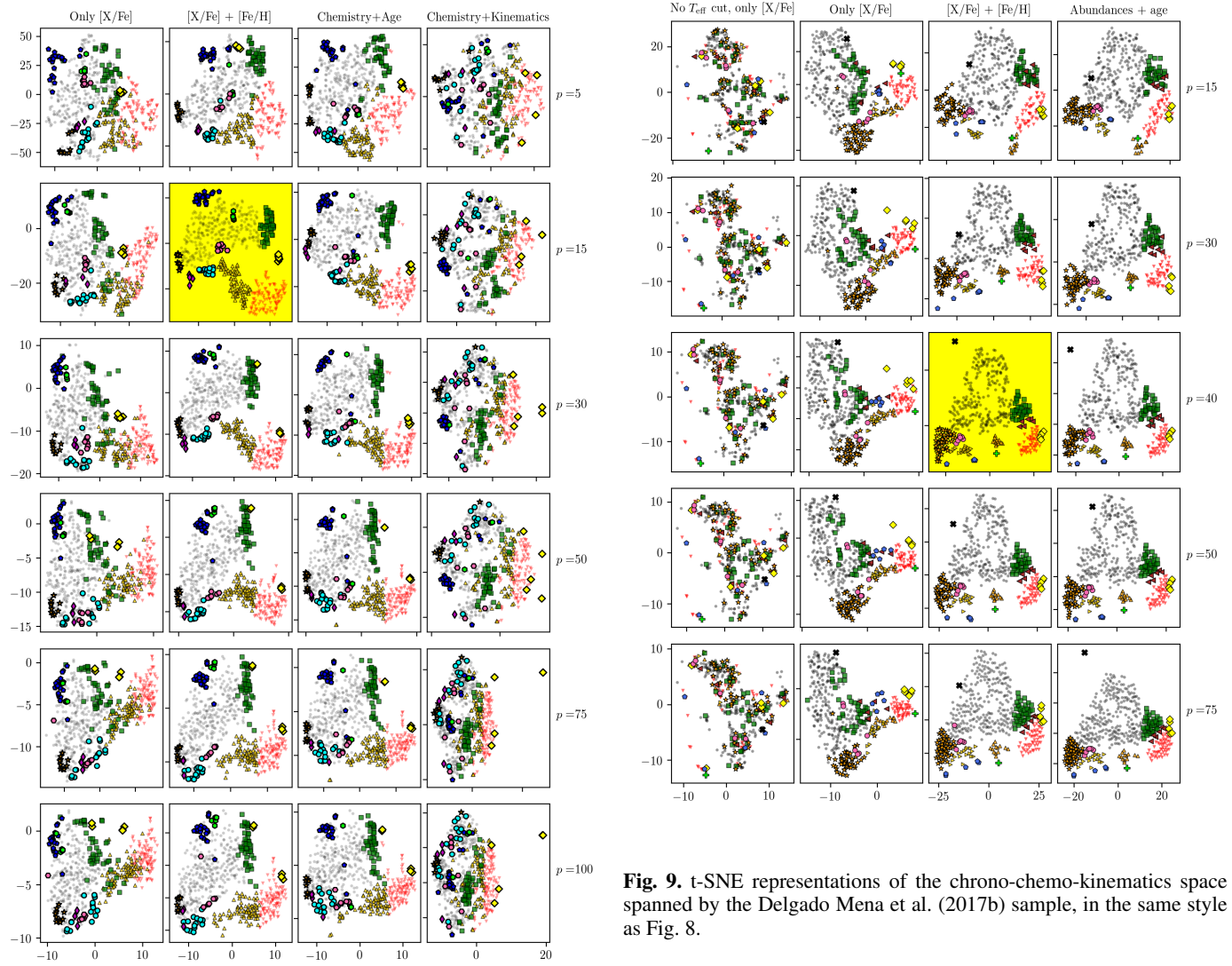


**Fig. 9.** t-SNE representations of the chrono-chemo-kinematics space spanned by the Delgado Mena et al. (2017b) sample, in the same style as Fig. 8.

**Fig. 8.** t-SNE representations of the chrono-chemo-kinematics space spanned by the Bensby et al. (2014) sample. Each column row represents a combination of input information, while each row corresponds to a particular perplexity value, as indicated on the right side of the figure. The panel highlighted in yellow represents the results that we analyse in detail in this paper by defining chemical subpopulations based on this map.